

# Chemical Science

Accepted Manuscript

This article can be cited before page numbers have been issued, to do this please use: L. Zhang, M. Xia, W. Li, S. Ren, L. Deng, S. Zhang, L. Huang, W. Song and X. Lu, *Chem. Sci.*, 2026, DOI: 10.1039/D6SC02482C.



This is an Accepted Manuscript, which has been through the Royal Society of Chemistry peer review process and has been accepted for publication.

Accepted Manuscripts are published online shortly after acceptance, before technical editing, formatting and proof reading. Using this free service, authors can make their results available to the community, in citable form, before we publish the edited article. We will replace this Accepted Manuscript with the edited and formatted Advance Article as soon as it is available.

You can find more information about Accepted Manuscripts in the [Information for Authors](#).

Please note that technical editing may introduce minor changes to the text and/or graphics, which may alter content. The journal's standard [Terms & Conditions](#) and the [Ethical guidelines](#) still apply. In no event shall the Royal Society of Chemistry be held responsible for any errors or omissions in this Accepted Manuscript or any consequences arising from the use of any information it contains.

# Interface Charge Engineering of Ternary RuCoMo Oxide Nanofibers toward High-Current-Density Water Electrolysis

Linfeng Zhang,<sup>a,1</sup> Mingze Xia,<sup>a,1</sup> Weimo Li,<sup>\*b</sup> Siyu Ren,<sup>a</sup> Li Deng,<sup>a</sup> Siqi Zhang,<sup>a</sup> Lin Huang,<sup>a</sup> Wei Song,<sup>c</sup> Xiaofeng Lu<sup>\*a</sup>

<sup>a</sup>Alan G. MacDiarmid Institute, College of Chemistry Jilin University Changchun 130012, P.R. China. E-mail: xflu@jlu.edu.cn

<sup>b</sup>Department of Materials Science and Engineering, Zhejiang Normal University Yingbin Road 688, Jinhua 321004, P. R. China. Email: liweimo@zjnu.edu.cn

<sup>c</sup>State Key Laboratory of Supramolecular Structure and Materials, College of Chemistry, Jilin University, Changchun 130012, P. R. China

† Electronic supplementary information (ESI) available.

<sup>1</sup>These authors contribute equally to this work.

## Abstract

The efficacy of RuO<sub>2</sub> as a bifunctional electrocatalyst for alkaline water electrolysis is usually constrained by its sluggish hydrogen evolution kinetics and poor stability. Herein, we report the fabrication of ternary RuCoMoO<sub>x</sub> nanofibers (NFs) incorporating oxide heterojunctions, which address these issues through interfacial charge engineering. The electron redistribution induced by the constructed interface optimizes the local electronic environment, endowing the catalyst with superior activity and stability for both the hydrogen and oxygen evolution reactions (HER/OER). The RuCoMoO<sub>x</sub> NFs achieve ultralow overpotentials of 274.8 mV for HER and 367.9 mV for OER to deliver a high current density of 1 A cm<sup>-2</sup>, surpassing commercial Pt/C and RuO<sub>2</sub> benchmarks. Moreover, the catalyst possesses superior operational stability for both HER and OER at 1 A cm<sup>-2</sup> compared to Pt/C and RuO<sub>2</sub>, respectively. In a practical electrolyzer, the assembled symmetric RuCoMoO<sub>x</sub> NFs||RuCoMoO<sub>x</sub> NFs system delivers a much lower working voltage than Pt/C||RuO<sub>2</sub> and maintains stable operation at 1 A cm<sup>-2</sup> for 60 h. This work validates interfacial charge engineering as a key strategy



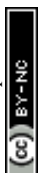
for creating high-performance noble-metal-lean electrocatalysts for industrial water electrolysis.

View Article Online  
DOI: 10.1039/D6SC02482C

## Introduction

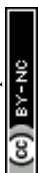
The global energy crisis and the exacerbation of climate change, driven by greenhouse gas emissions from excessive fossil fuel consumption, have intensified the demand for sustainable low-carbon energy alternatives.<sup>1-3</sup> In this context, electrochemical water splitting powered by renewable electricity has consequently emerged as a pivotal carbon-neutral technology for hydrogen (H<sub>2</sub>) production. The efficiency of this process is governed by the hydrogen evolution reaction (HER) and the oxygen evolution reaction (OER), placing critical demands on the development of highly efficient and robust electrocatalysts.<sup>4,5</sup> Although noble metal-based catalysts (e.g., Pt/C and IrO<sub>2</sub>) currently dominate industrial electrocatalytic water splitting, their prohibitive costs and limited availability severely restrict widespread implementation. Therefore, the development of cost-effective and sustainable alternatives has become an urgent priority.<sup>6,7</sup>

To address the cost and scarcity constraints of noble metal-based catalysts, recent research has focused on innovative designs that minimize noble metal loading while maintaining or even enhancing catalytic performance.<sup>8,9</sup> Strategies such as interface engineering and crystal-phase modulation enable atomic-level electronic structure tailoring, generating highly active sites with enhanced catalytic functionality.<sup>10-12</sup> In particular, heterojunction construction promotes interfacial charge redistribution, which optimizes the electronic environment of the catalyst and improves its intrinsic activity. The synergistic effects between components often yield performance enhancement that surpass those of individual-component catalysts.<sup>13-15</sup> Among various candidate materials, ruthenium-based oxides (e.g., RuO<sub>2</sub>) have attracted significant interest due to their exceptional alkaline OER activity, yet face deployment barriers from high cost and insufficient stability under industrial current density.<sup>16-18</sup> In contrast, CoMoO<sub>4</sub> presents a cost-effective alternative for OER, featuring multivalent

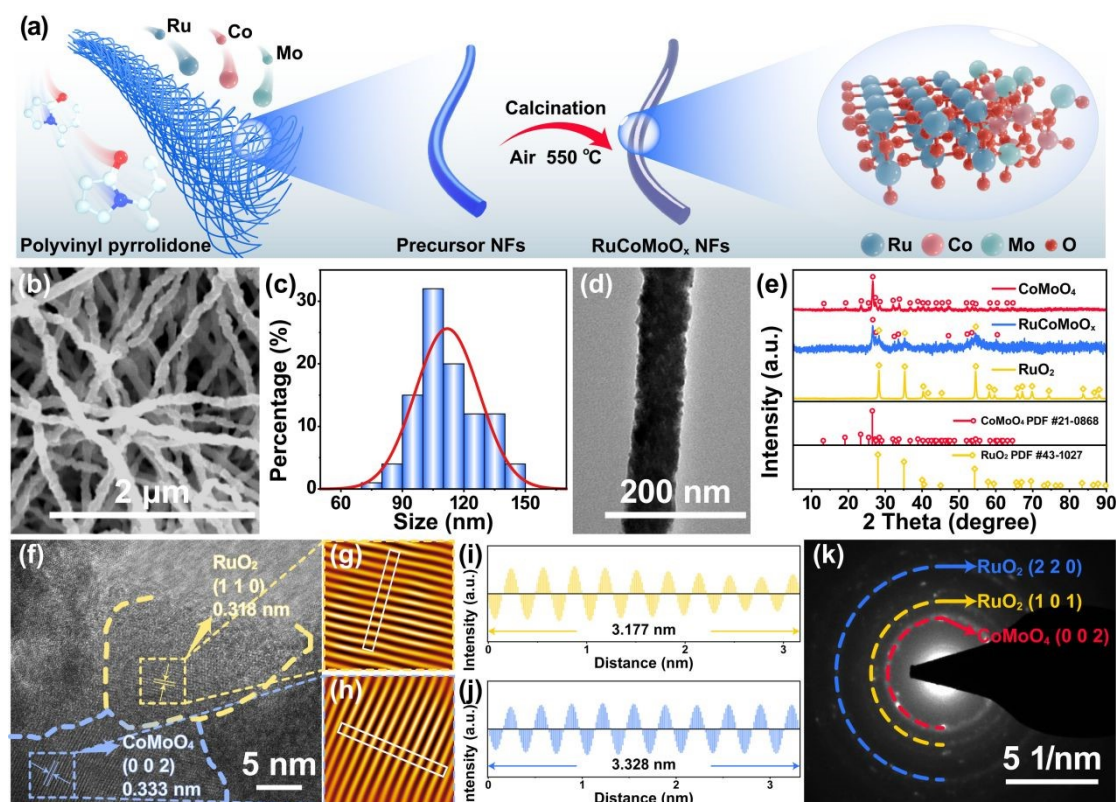


characteristic, a tunable electronic structure, and favorable intermediate adsorption energetics.<sup>19–21</sup> Although  $\beta$ -CoMoO<sub>4</sub> has been fabricated via a hydrothermal method and exhibits a favorable OER activity with an overpotential of 366 mV at 10 mA cm<sup>-2</sup> in alkaline electrolyte, its OER activity remains intrinsically lower than that of noble-metal catalysts. Furthermore, its HER performance is limited by suboptimal H\* adsorption energetics. Consequently, the implementation of CoMoO<sub>4</sub> as a bifunctional catalyst for overall water splitting remains constrained.<sup>22</sup>

Herein, we propose an interfacial engineering strategy to construct ternary RuCoMoO<sub>x</sub> nanofibers (NFs) featuring RuO<sub>2</sub>/CoMoO<sub>4</sub> heterojunctions as a bifunctional electrocatalyst for water electrolysis. This design leverages interfacial electronic interactions and synergistic effects to achieve highly efficient and stable electrocatalytic performance. This unique configuration not only exposes abundant catalytically active interfaces that facilitate rapid charge transfer and redistribution, thereby optimizing the electronic states of the active sites, but also benefits from the continuous fibrous morphology to promote efficient axial electron transport along the NFs. The synergistic interplay endows RuCoMoO<sub>x</sub> NFs with remarkable bifunctional activity in alkaline media, achieving ultralow overpotentials of only 274.8 mV for HER and 367.9 mV for OER at 1 A cm<sup>-2</sup>, along with outstanding industrial stability. When assembled into a RuCoMoO<sub>x</sub> NFs||RuCoMoO<sub>x</sub> NFs electrolyzer for overall water splitting (OWS), the system delivers a much lower working voltage and more robust operation than commercial Pt/C||RuO<sub>2</sub> counterpart. Density functional theory (DFT) calculations reveal that substantial electron redistribution across the RuO<sub>2</sub>/CoMoO<sub>4</sub> interface effectively activates Co sites for OER while optimizing Ru sites for HER, thereby reducing the kinetic barriers and enhancing overall catalytic activity. This work demonstrates that coupling interfacial charge engineering with nanofibrous architecture can overcome the limitations of single-metal oxides, providing a viable path to noble metal-lean electrocatalysts that meet industrial-current-density requirements for both activity and durability in alkaline water electrolysis.



## Result and discussion

View Article Online  
DOI: 10.1039/D6SC02482C

**Fig. 1.** (a) Schematic illustration of the synthetic procedure for RuCoMoO<sub>x</sub> NFs. (b) SEM image, (c) fiber diameter distribution, and (d) TEM image of RuCoMoO<sub>x</sub> NFs. (e) XRD patterns of CoMoO<sub>4</sub> NFs, RuCoMoO<sub>x</sub> NFs, and RuO<sub>2</sub> NFs. (f) HRTEM image of RuCoMoO<sub>x</sub> NFs with fast Fourier transform (FFT) patterns and lattice fringes of (g, i) RuO<sub>2</sub> (110) and (h, j) CoMoO<sub>4</sub> (002) crystal planes. (k) SAED pattern of RuCoMoO<sub>x</sub> NFs.

Electrospinning offers a versatile strategy that enables the fabrication of nanofibers.<sup>23–25</sup> As depicted in Fig. 1a, precursor NFs containing RuCl<sub>3</sub>, Co(NO<sub>3</sub>)<sub>2</sub>, and molybdenum acetylacetonate dispersed in a polyvinylpyrrolidone (PVP) matrix are fabricated via electrospinning, yielding a uniform fibrous structure with an average diameter of approximately 198.8 nm (Fig. S1, ESI†). After calcination at 550 °C, field-emission scanning electron microscope (FESEM) and transmission electron microscopy (TEM) images show sintering-induced shrinkage of the resulting RuCoMoO<sub>x</sub> NFs, with the average diameter decreasing to 111.9 nm, attributable to the decomposition of PVP (Fig. 1b-d). Meanwhile, deliberate variation of the Ru molar



content in RuCoMoO<sub>x</sub> NFs shows that the uniform nanofibrous morphology is maintained across all compositions (Fig. S2–S5, ESI†). In addition, a systematic investigation of the calcination temperature reveals that increasing the temperature from 450 °C to 650 °C leads to significantly enhanced surface roughness of the nanofibers (Fig. S6 and S7, ESI†). X-ray diffraction (XRD) pattern of RuCoMoO<sub>x</sub> NFs confirms the presence of both tetragonal RuO<sub>2</sub> (JCPDS No. 43-1027) and monoclinic CoMoO<sub>4</sub> (JCPDS No. 21-0868), providing evidence for the successful formation of the RuO<sub>2</sub>/CoMoO<sub>4</sub> composite (Fig. 1e).<sup>26–28</sup> With increasing Ru precursor loading, the intensity of the RuO<sub>2</sub> diffraction peaks increases proportionally, indicating a higher phase fraction of RuO<sub>2</sub> (Fig. S8a, ESI†). At a fixed Ru:Co:Mo molar ratio of 1:1:1, raising the calcination temperature from 450 °C to 650 °C results in progressively sharper and more intense diffraction peaks, reflecting improved crystallinity and larger average crystallite sizes (Fig. S8b, ESI†). In addition, N<sub>2</sub> adsorption–desorption isotherm demonstrates that the RuCoMoO<sub>x</sub> NFs exhibits a Brunauer–Emmett–Teller (BET) surface area of 24.88 m<sup>2</sup> g<sup>-1</sup> (Fig. S9, ESI†), which is similar with the previous reported electrospun nanofibers.<sup>29,30</sup>

High-resolution TEM (HRTEM) imaging of the RuCoMoO<sub>x</sub> NFs reveals distinct lattice fringes with measured spacings of 0.318 nm and 0.333 nm (Fig. 3f), which are assigned to the (110) plane of RuO<sub>2</sub> and the (002) plane of CoMoO<sub>4</sub>, respectively. The formation of a well-defined heterointerface between these two phases is evidenced, supported further by the corresponding fast Fourier transform (FFT) analyses (Fig. 1g–j).<sup>31–33</sup> Additionally, the selected area electron diffraction (SAED) pattern displays characteristic diffraction rings indexed to the (101) and (200) planes of RuO<sub>2</sub> alongside the (002) facet of CoMoO<sub>4</sub> (Fig. 1k). Energy-dispersive X-ray (EDX) analysis confirms the elemental composition of the as-prepared RuCoMoO<sub>x</sub> NFs, with C, Cu, and Si signals originating from the TEM grid and instrumentation (Fig. S10, ESI†). The EDX result further shows that the molar ratio of Ru:Co:Mo is 9.21:9.64:8.21, which is nearly identical to their feeding ratio. Collectively, these complementary structural characterizations collectively validate the successful integration of



RuO<sub>2</sub>(110)/CoMoO<sub>4</sub>(002) heterojunctions into the RuCoMoO<sub>x</sub> NFs, providing a robust structural basis for exploring interfacial electronic redistribution and its influence on electrocatalytic performance.

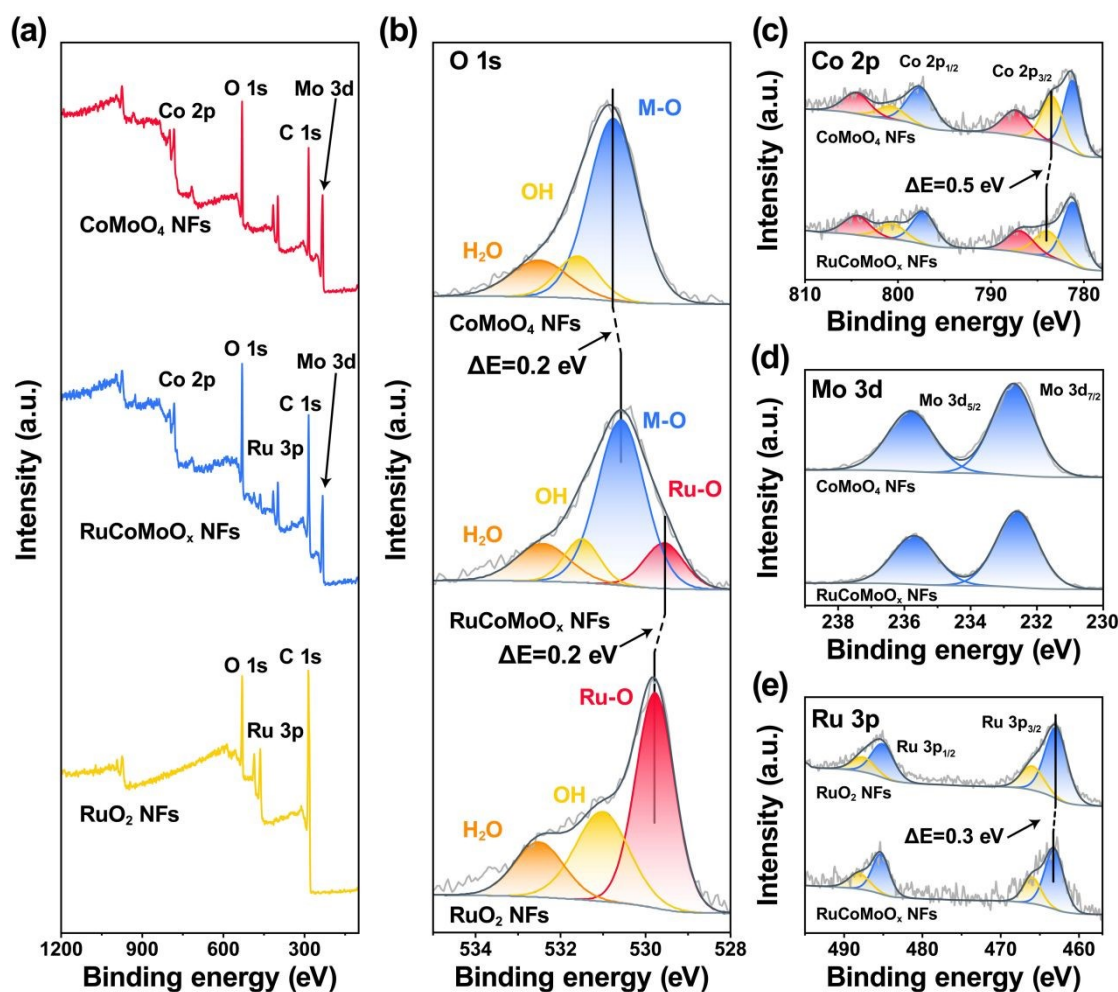
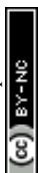


**Fig. 2.** XPS analysis of CoMoO<sub>4</sub> NFs, RuCoMoO<sub>x</sub> NFs, and RuO<sub>2</sub> NFs: (a) survey spectra, (b) high-resolution O 1s spectra. High-resolution spectra of (c) Co 2p for CoMoO<sub>4</sub> NFs and RuCoMoO<sub>x</sub> NFs, (d) Mo 3d for CoMoO<sub>4</sub> NFs and RuCoMoO<sub>x</sub> NFs, and (e) Ru 3p for RuO<sub>2</sub> NFs and RuCoMoO<sub>x</sub> NFs.

To gain deeper insight into the surface chemical states and interfacial electronic interactions within the catalysts, X-ray photoelectron spectroscopy (XPS) analysis is conducted. The survey spectra (Fig. 2a) confirm the successful incorporation of all constituent elements into the catalysts. In the O 1s region (Fig. 2b), RuCoMoO<sub>x</sub> NFs exhibit two distinct peaks centered at 530.6 eV and 529.6 eV, which correspond to the



lattice oxygen in  $\text{CoMoO}_4$  and  $\text{RuO}_2$ , respectively.<sup>19,34</sup> Notably, the binding energies of these lattice oxygen peaks are negatively shifted by 0.2 eV compared to pure  $\text{CoMoO}_4$  and  $\text{RuO}_2$ . These negative shifts suggest significant interfacial charge redistribution, providing further evidence of strong electronic interactions between  $\text{CoMoO}_4$  and  $\text{RuO}_2$  within the heterostructure. The high-resolution Co 2p spectrum of pristine  $\text{CoMoO}_4$  NFs displays the coexistence of  $\text{Co}^{2+}$  and  $\text{Co}^{3+}$  species, with corresponding peaks located at 781.2 eV and 783.4 eV, respectively. In the  $\text{RuCoMoO}_x$  NFs heterostructure, the  $\text{Co}^{2+}$  2p<sub>3/2</sub> peak shifts positively by 0.5 eV to 783.9 eV relative to that of  $\text{CoMoO}_4$  NFs, reflecting an altered electronic environment of  $\text{Co}^{2+}$  resulting from interfacial charge redistribution at the  $\text{CoMoO}_4/\text{RuO}_2$  heterojunction (Fig. 2c).<sup>35,36</sup> For the Mo 3d region, both  $\text{CoMoO}_4$  NFs and  $\text{RuCoMoO}_x$  NFs exhibit only  $\text{Mo}^{6+}$  signals, with the Mo 3d<sub>5/2</sub> and Mo 3d<sub>3/2</sub> peaks at 232.5 eV and 235.6 eV, respectively. No significant binding energy shift is observed between the two samples (Fig. 2d).<sup>37-40</sup> The Ru 3p spectrum of pristine  $\text{RuO}_2$  NFs features characteristic  $\text{Ru}^{4+}$  peaks at 462.9 eV (Ru 3p<sub>3/2</sub>) and 485.1 eV (Ru 3p<sub>1/2</sub>).<sup>41,42</sup> Upon heterostructure formation, the Ru 3p<sub>3/2</sub> peak shifts positively by 0.3 eV positive shift, indicating a modified electronic environment of Ru arising from interfacial charge redistribution at the  $\text{RuO}_2/\text{CoMoO}_4$  heterojunction (Fig. 2e).<sup>43,44</sup> Collectively, these XPS findings provide unambiguous evidence that the formation of  $\text{RuO}_2/\text{CoMoO}_4$  heterojunction induces charge redistribution, which effectively modulates the local electronic environment of the active sites, being responsible for the enhanced electrocatalytic activity.



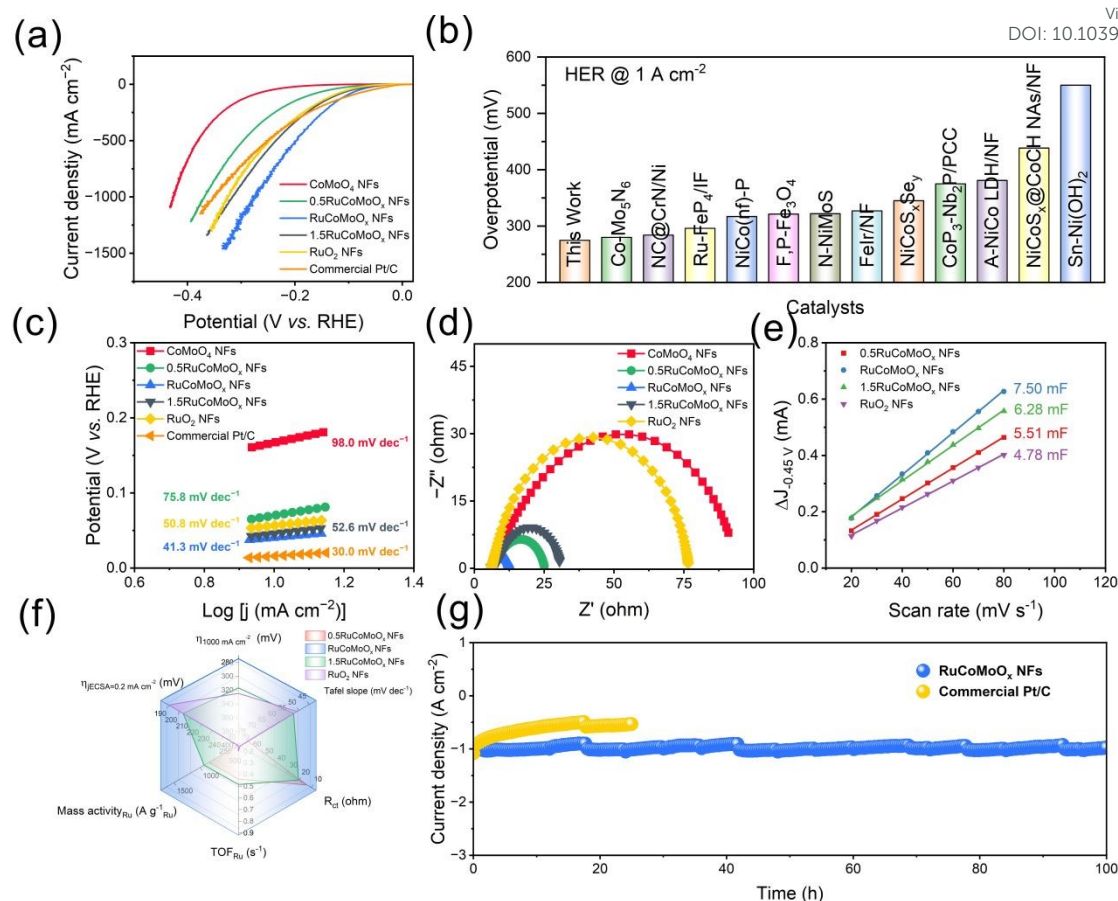


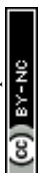
**Fig. 3.** HER performance in 1.0 M KOH. (a) LSV curves. (b) Performance comparison against state-of-the-art catalysts at 1 A cm<sup>-2</sup>. (c) Tafel plots. (d) Nyquist plots. (e)  $C_{dl}$  values and (f) radar chart of RuCoMoO<sub>x</sub> NFs and control catalysts. (g)  $I-t$  curves of RuCoMoO<sub>x</sub> NFs and commercial Pt/C conducted at 1 A cm<sup>-2</sup>.

We systematically evaluated the electrocatalytic HER performance of RuCoMoO<sub>x</sub> NFs alongside several control samples in 1.0 M KOH. Linear sweep voltammetry (LSV) profiles clearly demonstrate that RuCoMoO<sub>x</sub> NFs exhibit the optimal HER property, achieving a current density of 1 A cm<sup>-2</sup> with an overpotential of only 274.8 mV, significantly lower than those of CoMoO<sub>4</sub> NFs (425.2 mV), 0.5RuCoMoO<sub>x</sub> NFs (368.5 mV), 1.5RuCoMoO<sub>x</sub> NFs (317.0 mV), RuO<sub>2</sub> NFs (324.9 mV), and commercial Pt/C (347.7 mV) (Fig. 3a). Optimization of the calcination temperature further confirms that RuCoMoO<sub>x</sub> NFs treated at 550 °C afford the best HER activity (Fig. S11, ESI†). When benchmarked against recently reported HER electrocatalysts, RuCoMoO<sub>x</sub> NFs catalyst



ranks among the top performers in terms of overpotential at  $1 \text{ A cm}^{-2}$ , highlighting its exceptional activity (Fig. 3b, Table S1, ESI†). Tafel analysis indicates superior HER kinetics for RuCoMoO<sub>x</sub> NFs, with a Tafel slope of  $41.3 \text{ mV dec}^{-1}$ , approaching that of commercial Pt/C ( $30.0 \text{ mV dec}^{-1}$ ) (Fig. 3c). Electrochemical impedance spectroscopy (EIS) further supports these findings, with the Nyquist plot of RuCoMoO<sub>x</sub> NFs exhibiting the smallest charge transfer resistance ( $R_{ct}$ ) among the samples, suggesting the most rapid electron transfer kinetics (Fig. 3d). The EIS data are modeled using the equivalent circuits shown in Fig. S12, ESI†. The Bode plot (Fig. S13, ESI†) reveals distinct phase angle features, with the low-frequency region corresponding to the Volmer step and the mid-frequency region to the Heyrovsky step.<sup>45,46</sup> In addition, as the applied voltage decreases, the phase angle peaks in both the low- and mid-frequency regions progressively shift toward higher frequencies. This behavior is primarily ascribed to a reduction in charge transfer impedance at the catalyst surface/electrolyte interface and the acceleration of the interfacial reaction kinetics.<sup>47,48</sup>

The electrochemical active surface area (ECSA) is estimated from double-layer capacitance ( $C_{dl}$ ) measurements derived from cyclic voltammogram (CV) recorded at various scan rates (Fig. 3e, Fig. S14 and S15, ESI†). RuCoMoO<sub>x</sub> NFs exhibit the largest  $C_{dl}$  value of  $7.50 \text{ mF}$ , corresponding to the highest ECSA value (Table S2). Concurrently, the specific activity of the catalyst is assessed by analyzing ECSA-normalized LSV curves. Among all samples, RuCoMoO<sub>x</sub> NFs show a favorable overpotential of  $182.4 \text{ mV}$  at a normalized current density of  $0.2 \text{ mA cm}^{-2}_{ECSA}$ , indicating that the high intrinsic activity originates from the formation of the heterointerface (Fig. S16 and S17, ESI†). Furthermore, RuCoMoO<sub>x</sub> NFs exhibit superior mass activity<sub>Ru</sub> and the highest turnover frequency (TOF) per-Ru site (TOF<sub>Ru</sub>) at an overpotential of  $200 \text{ mV}$  (Fig. S18 and S19, ESI†), providing further evidence of accelerated HER kinetics and enhanced intrinsic catalytic activity. A radar chart summarizing six key HER performance metrics highlights the overall superiority of RuCoMoO<sub>x</sub> NFs (Fig. 3f). Long-term stability is assessed by chronoamperometry at  $1 \text{ A cm}^{-2}$  (Fig. 3g). Notably, the current density of RuCoMoO<sub>x</sub> NFs remains close to its



initial value after 100 h of testing, whereas commercial Pt/C exhibits a significant performance degradation after only 25 h. Post-test characterization confirms the structural and chemical stability of RuCoMoO<sub>x</sub> NFs. Specifically, FESEM, TEM and HRTEM images show that the nanofibrous morphology and chemical structure are well preserved (Fig. S20 and S21, ESI<sup>†</sup>). XRD reveals only a slight decrease in crystallinity, and XPS spectra indicate negligible changes in the chemical states of each element (Fig. S22, ESI<sup>†</sup>). Collectively, these results affirm the outstanding activity and stability of RuCoMoO<sub>x</sub> NFs as an efficient HER electrocatalyst.

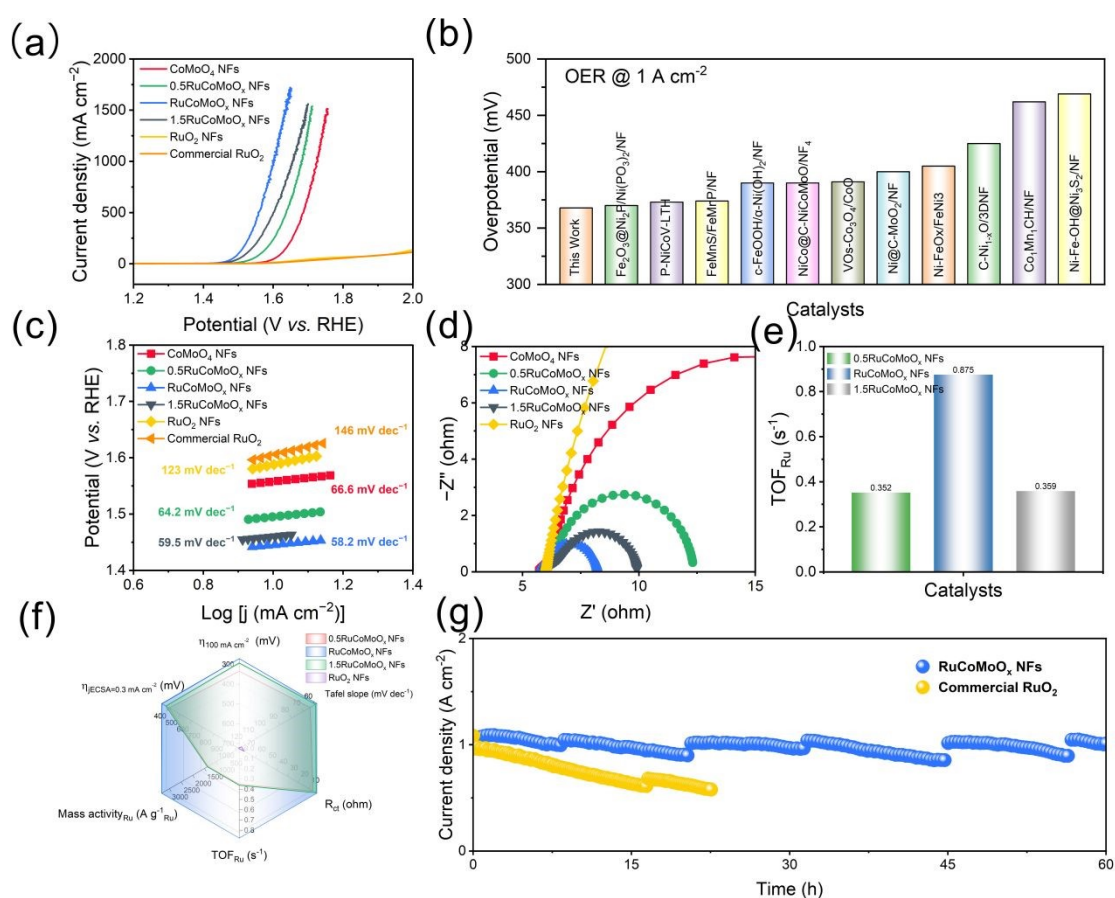
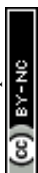


**Fig. 4.** OER performance in 1.0 M KOH. (a) LSV curves. (b) Performance comparison against state-of-the-art catalysts at 1 A cm<sup>-2</sup>. (c) Tafel plots. (d) Nyquist plots. (e) TOF values at η = 370 mV based on the Ru feeding content. (f) Radar chart of RuCoMoO<sub>x</sub> NFs and other control catalysts. (g) I-t curves of RuCoMoO<sub>x</sub> NFs and commercial RuO<sub>2</sub> conducted at 1 A cm<sup>-2</sup>.



Inspired by the enhanced HER performance achieved through interface engineering in RuCoMoO<sub>x</sub> NFs, the OER performance of the catalysts is also evaluated in alkaline media. Under optimized synthesis conditions, RuCoMoO<sub>x</sub> NFs calcined at 550 °C exhibits optimal OER activity, with an overpotential of 270.5 mV at 100 mA cm<sup>-2</sup>, considerably lower than those of CoMoO<sub>4</sub> NFs (393.4 mV), RuO<sub>2</sub> NFs (717.6 mV) and commercial RuO<sub>2</sub> (733.2 mV) (Fig. 4a and Fig. S23, ESI†). Remarkably, RuCoMoO<sub>x</sub> NFs require only 367.9 mV to reach an industrial-level current density of 1 A cm<sup>-2</sup>, surpassing most reported state-of-the-art alkaline OER catalysts (Fig. 4b and Table S3, ESI†). Furthermore, RuCoMoO<sub>x</sub> NFs show the lowest Tafel slope of 58.2 mV dec<sup>-1</sup> among the tested catalysts, indicating favorable OER kinetics (Fig. 4c). EIS further reveals that RuCoMoO<sub>x</sub> NFs possess the lowest R<sub>ct</sub> of 2.32 Ω, suggesting highly efficient electron transfer that underpins their outstanding OER performance (Fig. 4d). The Bode plot (Fig. S24, ESI†) shows that the smaller phase peak angle of RuCoMoO<sub>x</sub> NFs at low frequency region of the operando Bode phase plots indicates that, during the OER process, RuCoMoO<sub>x</sub> NFs with RuO<sub>2</sub>/CoMoO<sub>4</sub> heterojunctions exhibit faster charge transfer compared to RuO<sub>2</sub> NFs and CoMoO<sub>4</sub> NFs, leading to rapid OER kinetics.<sup>32,48</sup> The specific activity is assessed using ECSA-normalized LSV curves to investigate the intrinsic activity of catalysts. RuCoMoO<sub>x</sub> NFs demonstrate the highest intrinsic activity, with a low overpotential of 339.4 mV at 0.3 mA cm<sup>-2</sup><sub>ECSA</sub> (Fig. S25 and S26, ESI†). Moreover, RuCoMoO<sub>x</sub> NFs deliver the highest TOF<sub>Ru</sub> of 0.875 s<sup>-1</sup> at 370 mV and a mass activity of 3346.49 A g<sup>-1</sup><sub>Ru</sub> (Fig. 4e, Fig. S27 and Fig. S28, ESI†), reflecting accelerated OER kinetics and superior catalytic efficiency. Integration of six key metrics in the radar chart conclusively demonstrates the comprehensive superiority of RuCoMoO<sub>x</sub> NFs for OER (Fig. 4f). Long-term chronopotentiometry test at 1 A cm<sup>-2</sup> reveals excellent operational stability of the RuCoMoO<sub>x</sub> NFs, which retains a current density comparable to its initial value after 60 h, whereas commercial RuO<sub>2</sub> declines rapidly after 22.5 h under identical conditions (Fig. 4h). Post-stability characterizations further corroborate the structural and chemical robustness of RuCoMoO<sub>x</sub> NFs. SEM, TEM and HRTEM images show that the nanofibrous morphology and chemical



structure remain well preserved (Fig. S29 and S30, ESI<sup>†</sup>). XRD pattern indicates only a slight reduction in crystallinity without no phase transformation. XPS spectra confirm that the valence states of all elements remain essentially unchanged. (Fig. S31, ESI<sup>†</sup>). Collectively, these results firmly establish RuCoMoO<sub>x</sub> NFs as a highly efficient and durable OER electrocatalyst, demonstrating great potential as bifunctional catalyst for overall water splitting applications.

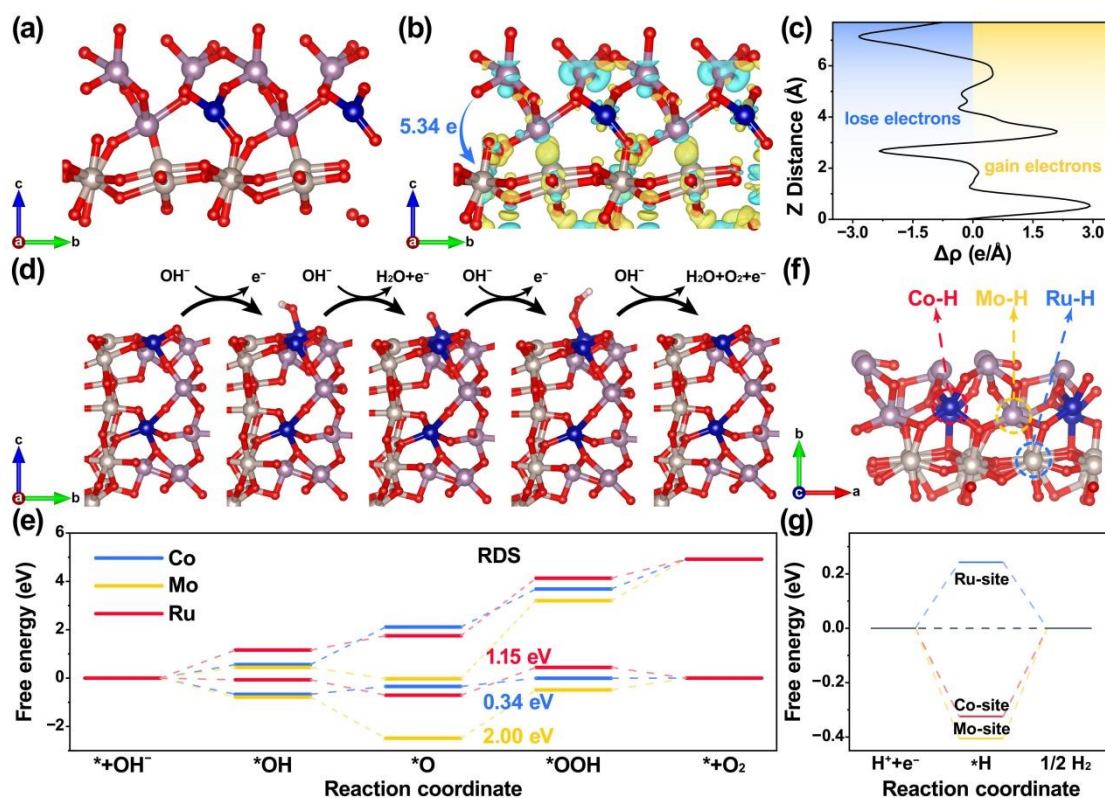
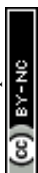


**Fig. 5.** DFT analysis of the RuO<sub>2</sub>/CoMoO<sub>4</sub> heterojunction. (a) Atomic structure of the RuO<sub>2</sub>/CoMoO<sub>4</sub> heterojunction model. (b) Differential charge density isosurfaces (yellow: charge accumulation; cyan: depletion). (c) Planar-averaged differential charge density along the z-axis. (d) Proposed OER reaction pathway on the heterojunction. (e) Calculated Gibbs free energy diagram for OER intermediates at U = 0 V and U = 1.23 V. (f) Atomic configurations of \*H adsorption sites. (g) Corresponding \*H adsorption free energies ( $\Delta G_{*H}$ ).

To elucidate the origin of the enhanced catalytic activity, systematic DFT calculations are conducted on a RuO<sub>2</sub> (110)/CoMoO<sub>4</sub> (002) heterojunction model (Fig.



5a). Differential charge density analysis demonstrates pronounced interfacial charge redistribution, characterized by electron accumulation on the RuO<sub>2</sub> side (yellow isosurfaces) and depletion on the CoMoO<sub>4</sub> side (cyan isosurfaces), confirming directional electron transfer from CoMoO<sub>4</sub> to RuO<sub>2</sub> across the heterojunction (Fig. 5b). Bader charge analysis quantifies this electron transfer as 5.34 e<sup>-</sup>, which is further corroborated by plane-averaged differential charge density profile along the Z-axis (Fig. 5c). Collectively, these results provide compelling evidence of substantial electronic structure modulation induced by heterojunction formation. The adsorption energies for the key OER intermediates (\*OH, \*O, \*OOH) are computed at Co, Mo and Ru sites on the RuO<sub>2</sub>/CoMoO<sub>4</sub> heterojunction (Fig. 5d). According to the Gibbs free-energy diagram, the Co site emerges as the most favorable active center for OER, where the transformation from \*O to \*OOH serves as the rate-determining step (RDS) with an energy barrier of only 0.34 eV, much lower than those at the Mo (2.00 eV) and Ru (1.15 eV) sites, accounting for the superior OER kinetics observed at the Co site (Fig. 5e). For HER, the Ru site exhibits a near-optimal H\* adsorption free energy ( $\Delta G_{*H} = 0.24$  eV), outperforming the Co (-0.32 eV) and Mo (-0.41 eV) sites, thereby enabling highly favorable \*H adsorption-desorption dynamics (Fig. 5f and g). Thus, the Co and Ru sites function as highly active centers for OER and HER, respectively. This site-specific functionalization, driven by interfacial charge engineering, underpins the exceptional synergistic bifunctional performance of the RuO<sub>2</sub>/CoMoO<sub>4</sub> heterojunction.



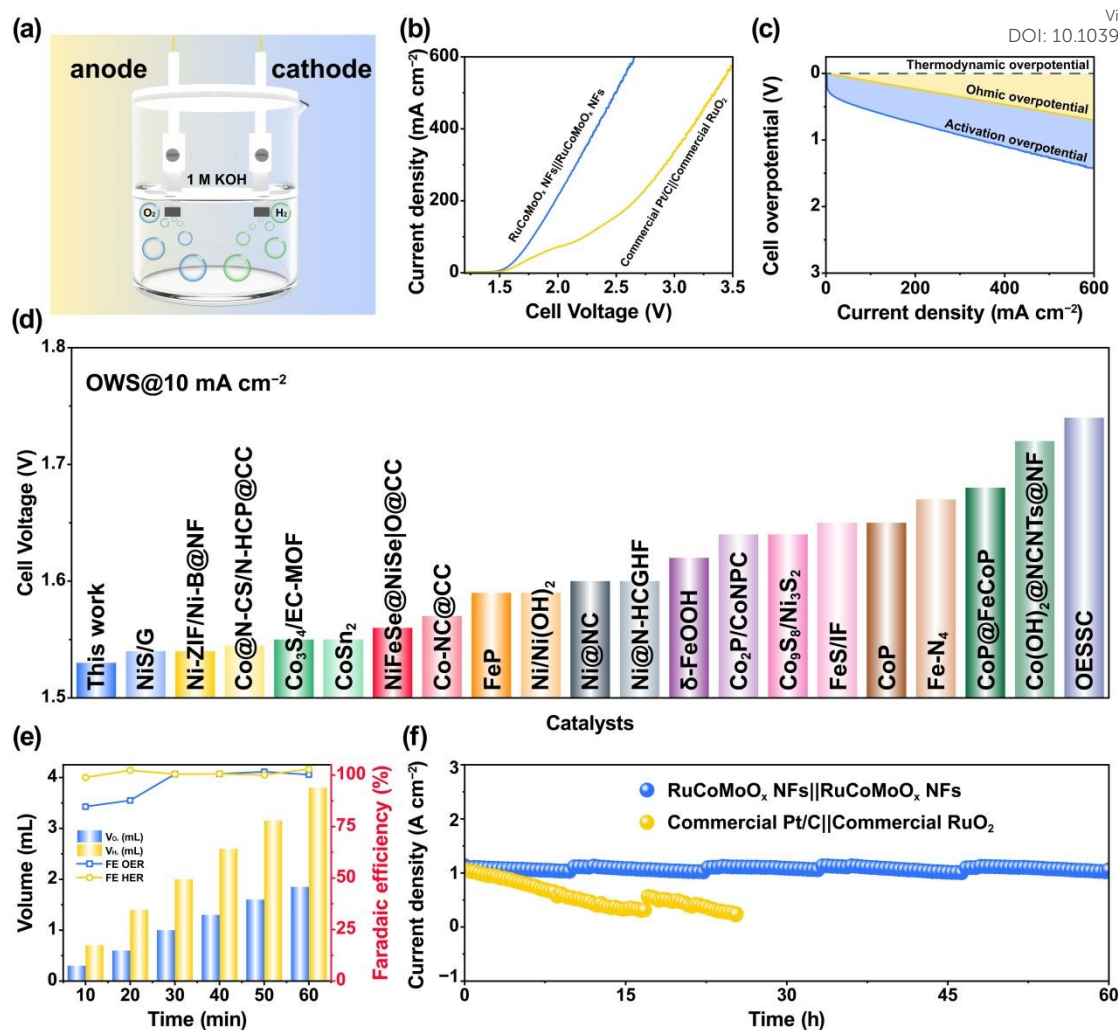


**Fig. 6.** Overall water splitting performance in a two-electrode system. (a) Schematic of the alkaline electrolyzer. (b) LSV curves of overall water splitting for RuCoMoO<sub>x</sub> NFs||RuCoMoO<sub>x</sub> NFs and commercial Pt/C||commercial RuO<sub>2</sub> electrolyzers. (c) Contributions of ohmic overpotential and activation overpotential. (d) Cell voltages required to achieve 10 mA cm<sup>-2</sup> compared with state-of-the-art alkaline electrolyzers. (e) FE of RuCoMoO<sub>x</sub> NFs||RuCoMoO<sub>x</sub> NFs electrolyzer. (f) Chronopotentiometric stability test of electrolyzers at 1 A cm<sup>-2</sup>.

To assess the OWS performance of the RuCoMoO<sub>x</sub> NFs under industrial current density conditions, a two-electrode electrolyzer is assembled using RuCoMoO<sub>x</sub> NFs as both the cathode and anode (Fig. 6a). The RuCoMoO<sub>x</sub> NFs||RuCoMoO<sub>x</sub> NFs electrolyzer requires only 1.53 V to reach 10 mA cm<sup>-2</sup>, significantly lower than the 1.58



V required by the commercial Pt/C||commercial RuO<sub>2</sub> electrolyzer (Fig. 6b). Furthermore, the RuCoMoO<sub>x</sub> NFs||RuCoMoO<sub>x</sub> NFs system exhibits superior activity, as evidenced by a smaller activation overpotential region compared to the commercial counterpart (Fig. 6c and Fig. S32a, ESI†). In addition, this configuration outperforms most reported bifunctional electrocatalysts-based electrolyzers (Fig. 6d and Table S4). The Faradaic efficiencies (FEs) for both HER and OER are measured at 100 mA cm<sup>-2</sup> using the water displacement method to assess the practical efficiency of the electrolyzer. The RuCoMoO<sub>x</sub> NFs||RuCoMoO<sub>x</sub> NFs system deliver FEs of 102.9% for HER and 100.2% for OER, surpassing those of the commercial Pt/C||commercial RuO<sub>2</sub> (101.3% for HER and 79.8% for OER), respectively (Fig. 6e and Fig. S32b, ESI†). Moreover, long-term stability tests conducted at an industrial current density of 1 A cm<sup>-2</sup> reveal that the RuCoMoO<sub>x</sub> NFs||RuCoMoO<sub>x</sub> NFs system retains stably in current density after 60 h of continuous operation. In contrast, the commercial Pt/C||commercial RuO<sub>2</sub> shows a significant reduction in its current density after more than 20 h under the identical conditions (Fig. 6f). These results underscore the outstanding durability and industrial applicability of the RuCoMoO<sub>x</sub> NFs-based water electrolysis for sustainable H<sub>2</sub> production.

## Conclusion

In summary, RuCoMoO<sub>x</sub> NFs incorporating RuO<sub>2</sub>/CoMoO<sub>4</sub> heterojunctions are successfully synthesized via electrospinning followed by controlled calcination. The optimized nanofibrous architecture facilitates efficient charge transfer, endowing the material with outstanding bifunctional activity, achieving ultralow overpotentials of 274.8 mV for HER and 367.9 mV for OER at 1 A cm<sup>-2</sup>, while maintaining excellent durability under such ampere-level current densities. When assembled into an alkaline electrolyzer, the RuCoMoO<sub>x</sub> NFs||RuCoMoO<sub>x</sub> NFs system requires only 1.53 V to deliver 10 mA cm<sup>-2</sup> and maintains stable current density after 60 h of operation under ampere-level conditions. DFT calculations reveal that interfacial electron redistribution across the RuO<sub>2</sub>/CoMoO<sub>4</sub> heterojunction optimizes the adsorption energetics of key



intermediates at Ru and Co sites, thereby enhancing the HER and OER performance, respectively. This study provides valuable design principles for developing robust noble-metal-lean Ru-based electrocatalysts that meet the practical demands of industrial alkaline water electrolysis.

View Article Online  
DOI: 10.1039/D6SC02482C

## Acknowledgements

This work was financially supported by the National Natural Science Foundation of China (52273056) and Science and Technology Development of Jilin Province, China (YDZJ202501ZYTS305).

## References

- 1 Z. W. Seh, J. Kibsgaard, C. F. Dickens, I. Chorkendorff, J. K. Nørskov and T. F. Jaramillo, *Science*, 2017, **355**, eaad4998.
- 2 J. Chow, R. J. Kopp and P. R. Portney, *Science*, 2003, **302**, 1528–1531.
- 3 L. Li, P. Wang, Q. Shao and X. Huang, *Chem. Soc. Rev.*, 2020, **49**, 3072–3106.
- 4 W. Li, C. Wang and X. Lu, *J. Mater. Chem. A*, 2021, **9**, 3786–3827.
- 5 W. Li, C. Wang and X. Lu, *Nano Lett.*, 2024, **24**, 11779–11792.
- 6 M. Rafique, T. Yao, S. Ma, Y. Xu, L. Li, J. Han, Q. Fu, W. Li, Z. Yuan, K. Wang and B. Song, *Adv. Funct. Mater.*, 2025, e12495.
- 7 J. Baek, M. D. Hossain, P. Mukherjee, J. Lee, K. T. Winther, J. Leem, Y. Jiang, W. C. Chueh, M. Bajdich and X. Zheng, *Nat. Commun.*, 2023, **14**, 5936.
- 8 K. B. Ibrahim, G. P. Darshan, G. Benetti, P. Kumar, E. Rodríguez-Castellón, T. A. Shifa, E. Moretti and A. Vomiero, *Adv. Sustainable Syst.*, 2025, 2500385.
- 9 W. Yang, Z. Wang, J. Zhang, L. Jia, J. Li, X. Chen, X. Liu, H. Zhang, J. Lin, M. Zhao and Q. Chen, *Angew. Chem. Int. Ed.*, 2025, **64**, e202509768.
- 10 H. He, D. Zhu, C. Huang, G. Chang, Y. Qian, M. Ran, A. Hu, X. Chen and Q. Tang, *ACS Appl. Mater. Interfaces*, 2025, **17**, 29535–29545.
- 11 K. Du, L. Zhang, J. Shan, J. Guo, J. Mao, C.-C. Yang, C.-H. Wang, Z. Hu and T.



- Ling, *Nat. Commun.*, 2022, **13**, 5448.
- 12 H. Xu, H. Shang, C. Wang and Y. Du, *Coord. Chem. Rev.*, 2020, **418**, 213374.
- 13 S. Fu, Y. Ma, X. Yang, X. Yao, Z. Jiao, L. Cheng and P. Zhao, *Appl. Catal., B*, 2023, **333**, 122813.
- 14 F. Luo, W. Liu, Y. Liu, P. Yu, X. Jiang and S. Chen, *Chem. Eng. J.*, 2023, **475**, 146140.
- 15 C. Xu, Y. Hong, Z. Li, X. Di, W. Wang, X. Dong and X. Mou, *Coord. Chem. Rev.*, 2025, **523**, 216287.
- 16 Y. Zhang, J. Dong, T. Sun, X. Zhang, J. Chen and L. Xu, *Small*, 2024, **20**, 2305889.
- 17 J. Wang, H. Yang, F. Li, L. Li, J. Wu, S. Liu, T. Cheng, Y. Xu, Q. Shao and X. Huang, *Sci. Adv.*, 2022, **8**, eabl9271.
- 18 Y. Liu, L. Wu, Y. Wang, L.-W. Shen, G. Tian, L. Cui, L. Qin, L. Zhou, Y. Zhang, F. Rosei and X.-Y. Yang, *ACS Nano*, 2025, **19**, 2715–2725.
- 19 B. Fei, Z. Chen, Y. Ha, R. Wang, H. Yang, H. Xu and R. Wu, *Chem. Eng. J.*, 2020, **394**, 124926.
- 20 K. Chi, X. Tian, Q. Wang, Z. Zhang, X. Zhang, Y. Zhang, F. Jing, Q. Lv, W. Yao, F. Xiao and S. Wang, *J. Catal.*, 2020, **381**, 44–52.
- 21 W. Jia, Q. Lu, T. Tian, G. Pan, R. Tan, B. He and J. Liu, *Nanoscale*, 2024, **16**, 18076–18085.
- 22 X. Zhong, Y. Chen, T. Gan, Y. Huang, J. Li and S. Zhang, *Nano Res.*, 2025, **18**, 94907204.
- 23 B. Shi and X. Lu, *Chem. Sci.*, 2025, **16**, 17568-17594.
- 24 N. Song, S. Ren, Y. Zhang, C. Wang and X. Lu, *Adv. Funct. Mater.*, 2022, **32**, 2204751.
- 25 L. Zhang, W. Li, S. Ren, W. Song, C. Wang and X. Lu, *Adv. Energy Mater.*, 2025, **15**, 2403136.
- 26 X. Yu, R. B. Araujo, Z. Qiu, E. Campos dos Santos, A. Anil, A. Cornell, L. G. M. Pettersson and M. Johnsson, *Adv. Energy Mater.*, 2022, **12**, 2103750.
- 27 W. Li, W. Gou, L. Zhang, M. Zhong, S. Ren, G. Yu, C. Wang, W. Chen and X. Lu,



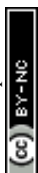
*Chem. Sci.*, 2024, **15**, 11890–11901.

View Article Online  
DOI: 10.1039/D6SC02482C

- 28 Y. Wang, Q. Jiang, S. Ren, J. Xu, Y. Wang, M. Zhong, and X. Lu, *Adv. Mater.*, 2025, **37**, 2504922.
- 29 X. Yu, M. Xia, R. Qi, Y. Wang, M. Gao, M. Zhong and X. Lu, *Chem. Sci.*, 2025, **16**, 10042-10050.
- 30 Q. Lin, R. Zhang, X. Zhang, S. Li, J. Dai, S. Li, Z. Wang, D. Liang, H. Fu and X. Zhang, *Catal. Lett.*, 2025, **155**, 67.
- 31 Y. Fan, W. Ma, J. He and Y. Du, *RSC Adv.*, 2017, **7**, 36193–36200.
- 32 W. Li, L. Zhang, L. Ma, J. Wang, R. Qi, Y. Pang, M. Xu, C. Zhao, C. Wang, M. Gao and X. Lu, *Nano Lett.*, 2025, **25**, 443–452.
- 33 Y. You, H. Chen, J. Guo, Z. Feng, J. Zhan, F. Yu and L.-H. Zhang, *Appl. Catal., B*, 2025, **363**, 124837.
- 34 H. Chen, X. Zhang, S. Geng, S. Song and Y. Wang, *Small Methods*, 2022, **6**, 2200636.
- 35 H. Wang, X. Shao, Y. Wei, X. Ai, J. Yu, N. Xiao, R. Gan and Y. Qu, *Appl. Catal., B*, 2025, **367**, 125110.
- 36 J. Zhang, Q. Chen, G. Wang, X. An, J. Zhang, Q. Liu, L. Xie, X. Li, W. Yao and Q. Kong, *Chem. Eng. J.*, 2024, **498**, 155474.
- 37 W. Jiang, M. Su, Y. Zheng and T. Fei, *ACS Appl. Mater. Interfaces*, 2024, **16**, 7406–7414.
- 38 W. Zhang, X. Xiao, L. Zheng and C. Wan, *Can. J. Chem. Eng.*, 2015, **93**, 1594–1602.
- 39 W. Tang, S. Zhu, H. Jiang, Y. Liang, Z. Li, S. Wu and Z. Cui, *J. Colloid Interface Sci.*, 2022, **625**, 606–613.
- 40 T. Chen, Y. Wu, H. Zhang, X. He, Z. Zhu, Y. Wei, C. Li, H. Zhu, S. Yu and W. Dong, *ACS Sustainable Chem. Eng.*, 2024, **12**, 9078–9090.
- 41 Y. Wang, X. Lei, B. Zhang, B. Bai, P. Das, T. Azam, J. Xiao and Z.-S. Wu, *Angew. Chem. Int. Ed.*, 2024, **63**, e202316903.
- 42 Y. Li, Q. Zhang, X. Zhao, H. Wu, X. Wang, Y. Zeng, Q. Chen, M. Chen and P. Liu,



- Adv. Funct. Mater.*, 2023, **33**, 2214124.
- 43 Y. Gao, D. Zheng, Q. Li, W. Xiao, T. Ma, Y. Fu, Z. Wu and L. Wang, *Adv. Funct. Mater.*, 2022, **32**, 2203206.
- 44 W. Li, R. Liu, G. Yu, X. Chen, S. Yan, S. Ren, J. Chen, W. Chen, C. Wang and X. Lu, *Small*, 2024, **20**, 2307164.
- 45 W. Chen, B. Wu, Y. Wang, W. Zhou, Y. Li, T. Liu, C. Xie, L. Xu, S. Du, M. Song, D. Wang, Y. Liu, Y. Li, J. Liu, Y. Zou, R. Chen, C. Chen, J. Zheng, Y. Li, J. Chen and S. Wang, *Energy Environ. Sci.*, 2021, **14**, 6428-6440.
- 46 H. Jin, X. Chen, Y. Da, L. Fan, R. Jiang, Y. Xiao, B. Yao, Q. He, Y. Yu and W. Chen, *J. Am. Chem. Soc.*, 2025, **147**, 3874-3884.
- 47 X. Zhao, H. Zheng, H. Sun, M. Chen, B. Wang, Q. Lu, B. Xiao, T. Zhou, D. Li, G. Qiu, J. Zhang, Y. Zhang, X. Xu, T. He and Q. Liu, *Adv. Energy Mater.*, 2026, **16**, e04983.
- 48 H. Sun, Z. Luo, M. Chen, T. Zhou, B. Wang, B. Xiao, Q. Lu, B. Zi, K. Zhao, X. Zhang, J. Zhao, T. He, J. Zhang, H. Cui, F. Liu, C. Wang, D. Wang and Q. Liu, *ACS Nano*, 2024, **18**, 35654-35670.



### Data availability statements

View Article Online  
DOI: 10.1039/D6SC02482C

The data supporting this article have been included as part of the Supplementary Information.

